Surface deformation and film corrugation during drying of polymer solutions induced by Marangoni phenomena

Stergios G. Yiantsios [a], Stefania K. Serpetsi [a], Frédéric Doumenc [b,c], Béatrice Guerrier [b]

[a] Department of Chemical Engineering, Aristotle University of Thessaloniki, Univ. Box 453, GR 541 24 Thessaloniki, Greece

[b] University Paris-Sud, CNRS, Lab FAST, Bat 502, Campus Universitaire, F-91405 Orsay, France

[c] Sorbonne Universités, UPMC Univ Paris 06, UFR919, F-75005 Paris, France

Corresponding author. Tel.: +30 2310 991293. E-mail address: yiantsio@auth.gr (S.G. Yiantsios).

Abstract

Solutal Marangoni phenomena occurring during drying of polymer solutions are investigated through numerical simulations. Bénard–Marangoni convection and free surface deformation are considered, taking into account the strong dependence of viscosity with solute concentration. Simulations show that free surface deformation which is resisted by capillary pressure reaches an overall magnitude that is proportional to the capillary number. Decreasing Ca also inhibits the interface deformation by favoring the formation of plumes that enhance mixing of the solute. For the range of capillary numbers corresponding to experiments, free surface deformation is not significant. However, Bénard–Marangoni convection induces non-uniformity of solute concentration and the varying viscosity leads to accumulation of solute at the periphery of convective cells that is observed up to the end of drying. Though simulations have been performed with dimensionless numbers significantly milder than the experimental ones, they are in agreement with experimental observations presented here and in the literature, suggesting that wrinkles may be viewed as the signature of Bénard–Marangoni convection.

Keywords: Marangoni effect, Free convection, Drying, Instability

1. Introduction

Marangoni phenomena have a wide range of manifestations, i.e. in crystal growth [1], heat or mass transfer enhancement [2], biological systems [3], thin film coatings and paints, etc. [4–8]. They have also been proposed as a possible cause for the development of organized structures in thin films with potentially promising properties for organic photovoltaics and photodiodes [9]. The most common factors inducing changes in surface tension, and thus Marangoni phenomena, are gradients of temperature or concentration of dissolved species and surfactants [10]. Theoretically, the mechanisms leading to hydrodynamic instabilities have been elucidated first by Pearson [11] for the surface-tension-driven flow (Bénard–Marangoni convection). Another instability mechanism due to surface deformation can also be present: it is known as the long-wave instability [12–14]. Earlier theoretical and experimental studies of thermocapillary phenomena are reviewed in [1,15]. Aspects particular to thin-film flows can be found in the reviews of Oron et al. [16] and Craster and Matar [17].

In the specific case of evaporating thin films, thermocapillary phenomena arise spontaneously because temperature gradients develop due to the energy transported through the film that is required to provide the latent heat for evaporation [18,19]. In multicomponent evaporating films surface tension gradients develop not only due to the effects of temperature but of species concentration as well. Several experimental studies confirm the influence of Marangoni phenomena, with stagnant or spin-coated films of various solutions where the volatile solvent invariably had lower surface tension than the solute [5,20–22]. Theoretical and numerical studies have also been devoted to the study of such configurations [6–8,23–27].

The present study is based on two previous and complementary approaches concerning solutal isothermal problems. On the one hand, theoretical analyses including linear stability and nonlinear simulations are presented in Serpetsi and Yiantsios' work [8]. They account for a deformable free surface but assume constant viscosity. Distinct modes of instability similar to those of Pearson [11] and Scriven and Sternling [12] were found. The former mode leads to cell development with minimal interfacial deformation, whereas the latter is oscillatory and induces significant interfacial deformation. Moreover, it was found that systems where the solute decreases the surface tension are also susceptible to instability in the form of a long-wavelength, non-oscillatory deformational mode. A related phenomenon of solutocapillary motion arises in the leveling of evaporating paints where a characteristic oscillatory behavior is observed. This has been explained by Overdiep [28] as a result of the synergistic action of capillary pressure and the concentration induced surface tension gradients.

On the other hand, linear stability analysis and direct numerical simulations have been performed by Doumenc et al. [26,27], taking into account the variation of viscosity with solute concentration, but disregarding the deformation of the interface. They focus on the onset of Bénard–Marangoni convection and point out the effect of varying viscosity. The aim of the present study is to bring together the two approaches and to get a view of the evolution of the interface deformation and concentration field during the drying, considering variable viscosity.

Indeed, one aspect particularly relevant to evaporating polymer solutions is the patterning of the final dried films, in the form of corrugations, wrinkles, pinholes, etc. [4]. Theoretical studies are virtually non-existent, except from a few that are limited to the long-wavelength approximation and the lubrication regime for the fluid flow and scalar transport [29,30]. The development of patterns in thin films encompasses a complex and multifaceted array of phenomena attributed to various factors. For some authors, a notable factor is the formation of an elastic skin and the incompatibility of its mechanical properties with those of the substrate or the lateral boundaries. Considerations and analyses along this line have been presented in the literature to explain various manifestations of wrinkling pattern development [31–33]. On a different length scale well known are phenomena of phase separation in polymer blends and in evaporating solutions [34–36]. However, Marangoni instabilities are also considered a potent factor that may lead to patterned dry films [5,21,35,37]. Notably, experiments performed by Bassou and Rharbi [5] with polystyrene/toluene solutions show a strong correlation between the convection cell morphology and the final corrugation of the dried film. From these observations, these authors infer that the final state of the film is the signature of solutal convection which redistributes the solute along the thin film, inducing lateral concentration non-uniformities, which might be finally frozen when most of the volatile solvent is removed by evaporation. Following this track, focus is placed in this paper on solutal Marangoni phenomena that could potentially be responsible for the wrinkling behavior observed in the experiments. Through numerical simulations, we explore the onset and development of solutal Bénard– Marangoni convection and consequently the development of concentration non-uniformities. We also investigate the deformation of the interface that could also results in corrugations if it is significant and continues until the end of the drying. The question addressed in this paper is therefore the relative importance of these two phenomena, according to values of capillary and Marangoni numbers, and the role played by viscosity variation with concentration.

The paper is organized as follows. First an experimental section presents some drying experiments performed with polyisobutylene/toluene solution, showing the drying and corrugation kinetics. Model assumptions, governing equations and numerical approach are developed in Section 3. The last section is devoted to the analysis of simulation results, focusing first on the free surface deformation and then on the solute distribution along the film.

Nomenclature

a_i	coefficient in experimental viscosity correlation [-]
Bo	Bond number [-]
$\boldsymbol{C}$	convection matrix for finite element diffusion equation [-]
Ca	capillary number [-]
D	mutual diffusion coefficient [m^2/s]
E	normalized evaporation velocity [-]
E'	volumetric evaporation rate [m/s]
$\boldsymbol{e_y}$	normalized unit vector in y-direction [-]
$\boldsymbol{G}$	matrix for pressure gradient terms of finite element momentum equation [-]
h	dimensionless local and instantaneous film thickness [-]
H_0	initial mean liquid film thickness [m]
$\boldsymbol{L}$	Laplacian matrix for finite element diffusion equation [-]
$\boldsymbol{L_2}$	matrix for viscous terms of finite element momentum equation [-]
M	Marangoni number [-]
$\boldsymbol{M}$	mass matrix for finite element diffusion equation [-]
$\boldsymbol{n}$	unit vector normal to the interface [-]
P	normalized liquid pressure [-]
P_0	pressure scale [Pa]
$\boldsymbol{S_1}$	boundary condition matrix for finite element diffusion equation [-]
$\boldsymbol{S_2}$	boundary condition matrix for finite element momentum equation [-]
Sc	Schmidt number [-]
t	time [s]
$\boldsymbol{u}$	normalized velocity [-]
U_0	Velocity scale [m/s]
$\boldsymbol{v_G}$	normalized grid velocity [-]
x	spatial coordinate [m]
y	spatial coordinate [m]

Greek symbols

Γ	normalized stress in scaling analysis [-]
$\Delta\sigma$	difference of solute and solvent surface tensions [N/m]
l	normalized wavelength of film thickness perturbations [-]
μ	normalized solution viscosity [-]
μ_0	initial solution viscosity [kg/m s]
ρ	solution density [kg/m^3]
σ_0	solvent surface tension [N/m]
$\boldsymbol{\tau}$	normalized viscous stress tensor [-]
ω	solute volume fraction [-]
$\boldsymbol{\omega}$	numerical vector of solute volume fraction nodal values [-]

Superscripts and subscripts

0	initial value
n	instantaneous value at nth time step
x	x-derivative
y	y-derivative
t	time derivative

2. Experimental

Drying experiments were performed as follows: polymer solution was poured in a glass dish (diameter about 0.11 m) and put on a balance located in an extracting hood at room temperature. The polymer/solvent solution is polyisobutylene/toluene. Polyisobutylene (PIB) was supplied by Sigma–Aldrich with $M_w = 5 \times 10^2$ kg/mol and polydispersity = 2.5. As is well known in polymer solutions, the viscosity strongly depends on solvent content. Fig. 1 displays the viscosity measurements for the PIB/toluene solution used in the experiments. An empirical law interpolated from measurements is used in the simulations of the present study, to describe the variation of viscosity with polymer concentration [27]: $log_{10}(\mu) = \sum_{i=0}^{4} \alpha_i Y^i$, with $Y = log_{10}(\varphi_{PIB})$, φ_{PIB} being the polymer volume fraction, and α = (8.235, 14.02, 6.575, 1.392, 0.1114).

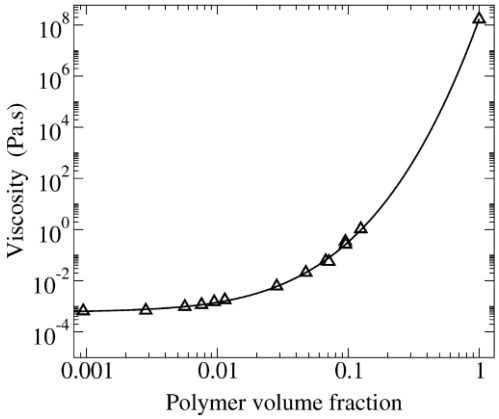

Fig. 1. Viscosity of PIB/toluene solution as a function of PIB volume fraction. Measurements (triangles, performed with a Low Shear 30 rheometer except for the viscosity of pure PIB) and empirical law used in the simulations (continuous line).

Mutual diffusion coefficient and solvent activity are also concentration dependent, but mainly for the concentrated regime and they can be assumed constant for polymer mass fraction less than about 0.6. There mutual diffusion coefficient is about 10^{-10} m^2/s and solvent activity is close to one [38]. Accordingly, after a short thermal transient regime, the evaporation flux is constant as long as the polymer mass fraction stays less than 0.6 [27]. Indeed, due to the thermodynamic behavior of

polymer solutions, the evaporation rate of the solution is similar to that of pure solvent even if the concentration of the solute increases at the free surface, as long as the polymer mass fraction does not reach 60% [38]. While both thermal and solutal instabilities may occur during the thermal transient regime [27], the temperature is uniform during the constant flux regime and thus only solutal convection is expected. At the end of this constant evaporation flux regime, the flux decreases due to solvent activity reduction. It is during this transition that, for some configurations (initial thickness and initial polymer concentration), corrugations of the surface appear and stay frozen in time. Typical time evolution of evaporation flux and of wrinkle invasion during the transition is shown in Fig. 2. Evaporation flux is derived from mass measurements performed during the drying experiment. Thanks to a camera located above the solution, the percentage of wavy surface is obtained through image processing of surface top views.

A quantitative estimation of the amplitude of the wrinkles was made using a Bruker Nano surface profilometer Dektak XT for the configuration corresponding to an initial thickness of 1.06 mm and an initial polymer volume fraction of 5.07%. Surface visualization is shown in Fig. 3, while Fig. 4 displays typical profiles. Standard deviation estimated on the whole surface is about 15 µm, the dry mean film thickness being about 54 µm. Another set of experiments have been performed by Bassou and Rharbi with PS/toluene solutions. Experimental conditions are close to the ones of the experiments on PIB/toluene. Viscosity also strongly increases with polymer concentration, but unlike PIB which is rubbery at room temperature, PS solution undergoes a glass transition when drying. However, the amplitude of wrinkles is quite similar for those two systems (cf. [5] for more details).

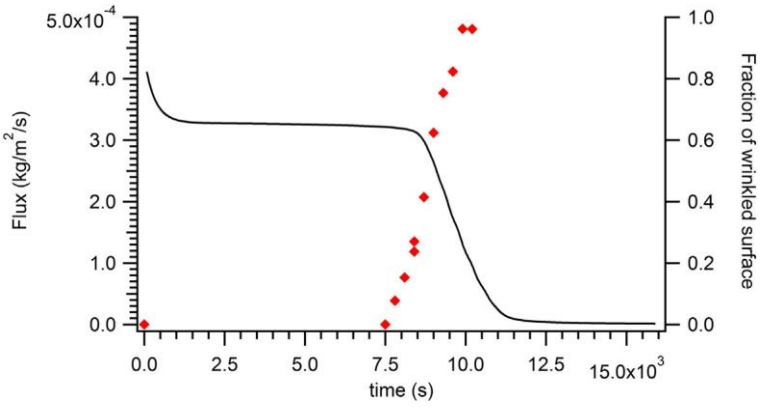

Fig. 2. Wrinkling of the film during the transition from the constant flux regime (t < 7500s) to the last regime (t > 11,000 s). Time evolution of the evaporative flux (continuous line, left axis) and time evolution of the percentage of wavy surface (diamond markers, right axis). After t = 11,000 s, wrinkling is frozen. The remaining flux, controlled by solvent diffusion in the concentrated solution, is very weak. (Configuration: initial thickness = 4 mm, initial polymer mass fraction = 5%, evaporation rate = 0.4 µm/s).

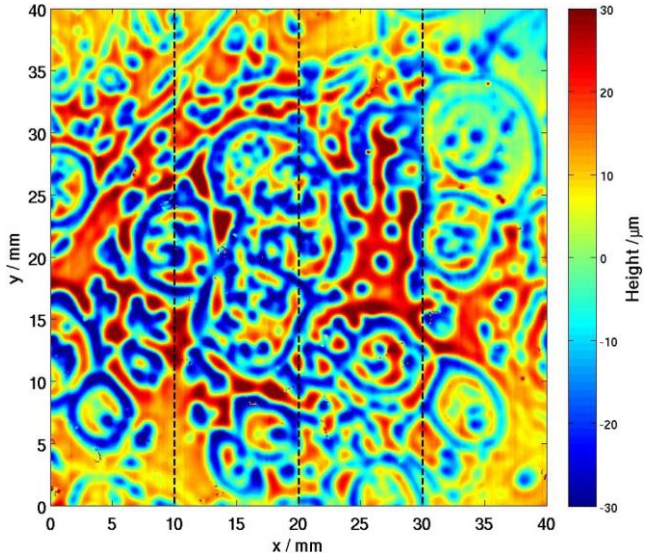

Fig. 3. Wrinkled dry polymer film. Image size is 40 mm × 40 mm. Color scale corresponds to film height, from blue color (holes) to red color (bumps). Zero level corresponds to the mean plane. (Configuration: initial thickness = 1.06 mm, initial polymer mass fraction = 5.07%, evaporation rate = 0.36 µm/s).

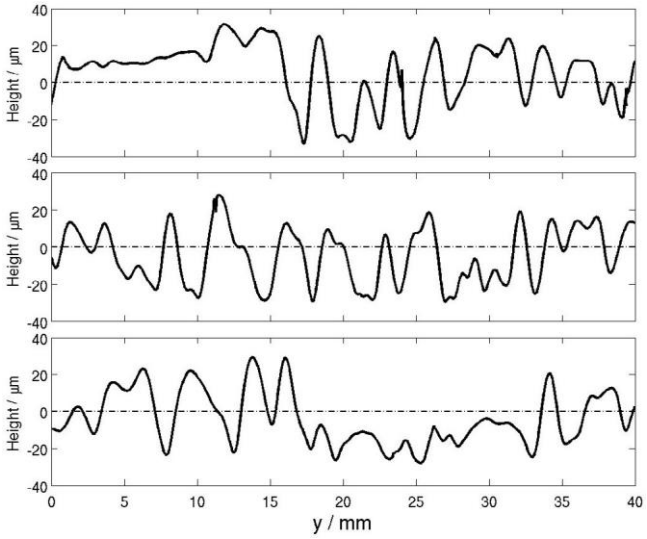

Fig. 4. Dry film profiles for $0 < y < 40$ mm and, from top to bottom, x = 10 mm, 20 mm, 30 mm (positions corresponding to dashed vertical lines in Fig.3.).

3. Mathematical and numerical formulation

3.1. Model assumptions and governing equations

The model adopted to describe the phenomena observed experimentally considers a Newtonian and incompressible liquid film containing dissolved polymer. The liquid viscosity is a strong function of polymer concentration. The film is resting on a flat horizontal substrate and the volatile solvent is evaporating in the overlying passive gaseous phase at a constant rate, E', corresponding to the constant evaporation flux regime described in the experimental section. Here E' is defined as a volumetric evaporation rate (mass rate divided by the liquid solvent density) and has dimensions of velocity. It is assumed that surface tension is a linear function of solute concentration and that the solute has a higher surface tension than the solvent. The initial transient thermal regime is disregarded and the problem is assumed isothermal.

The initial mean film thickness, H_0, is taken as the length scale and the initial solute volume fraction, ω_0, as a measure of concentration variations. Specific volumes of solute and solvent are assumed to be the same, so that no distinction is made between mass fraction and volume fraction and the solution density ρ is constant. Concentration is scaled by $\rho\omega_0$. If the difference between the surface tensions of solute and solvent is $\Delta\sigma$, then $\omega_0\Delta\sigma$ may be taken as characteristic measure of surface tension variations. Then, the balance of surface tension gradient forces with viscous stresses at the interface may be used to define a velocity scale, $U_0 = \omega_0\Delta\sigma/\mu_0$, where μ_0 is the initial viscosity of the solution. A viscous scaling for the pressure is adopted ($P_0 = \mu_0 U_0/H_0$). Then, the equations governing the fluid motion may be written in dimensionless form as follows [8]:

$$\frac{D\boldsymbol{u}}{Dt} = \frac{Sc}{M}[-\nabla P + \nabla.\mu(\nabla\boldsymbol{u} + \nabla\boldsymbol{u}^T)], \qquad (1)$$

which together with the continuity equation, $\nabla.\boldsymbol{u} = 0$, determine the velocity field. Here, Sc is the Schmidt number, defined as $Sc = \upsilon_0/D$, where the diffusivity, D, of the polymer in the solvent is assumed constant. M is the Marangoni number defined as

$$M = \frac{\omega_0\Delta\sigma\, H_0}{\mu_0 D}. \qquad (2)$$

The ratio M/Sc is essentially a Reynolds number for the flow and μ in Eq. (1) is the relative viscosity of the liquid, scaled by the initial one, μ_0. Since the Schmidt number is very large the inertia terms may be ignored and the flow can be described by the Stokes equations, as demonstrated in Appendix A with scaling arguments.

These equations are supplemented by the no-slip condition at the substrate and the stress condition at the interface

$$[-P\mathbf{I} + \boldsymbol{\tau}].\mathbf{n} = \left[\left(\frac{1}{Ca} + \omega\right)\nabla.\mathbf{n} - hBo\right]\mathbf{n} + \nabla_s\omega. \qquad (3)$$

Here τ is the viscous stress tensor of the liquid, $\boldsymbol{n}$ the normal vector to the interface pointing towards the gas, ω the dimensionless polymer mass fraction, and h the local dimensionless film thickness. Ca is the capillary number defined as

$$Ca = \frac{\mu_0 U_0}{\sigma_0} = \frac{\omega_0\Delta\sigma}{\sigma_0}, \qquad (4)$$

and Bo is a modified Bond number

$$Bo = \frac{\rho g h_0^2}{\Delta\sigma} \qquad (5)$$

quantifying the effects of gravity. Such effects are ignored in the present simulations assuming relatively thin films and weak gravity forces compared to the Marangoni forces. The first term on the right-hand-side of Eq. (3) corresponds to the capillary pressure, expressed through the curvature, $\nabla.\boldsymbol{n}$, and the last one corresponds to the Marangoni stresses, expressed through the surface gradient operator, ∇_s.

The liquid domain is shrinking due to evaporation and may also be deforming due to the flow. Its evolution is described by the kinematic condition, which written in terms of the instantaneous local thickness, h, has the form

$$(-h_t - uh_x + v)(1 + h_x^2)^{-1/2} = E, \qquad (6)$$

u and v are the horizontal and vertical component of the velocity. Here, the dimensionless parameter E, defined as $E = E'/U_0$, is the ratio of the time scales for motion due to Marangoni effects and for evaporation. If such effects are to be manifested, E has to be a small parameter.

Obviously, there is coupling between the flow and the distribution of the solute, the transport of which is described by the species conservation equation:

$$\frac{\partial \omega}{\partial t} + \boldsymbol{u}.\nabla\omega = \frac{1}{M}\nabla^2\omega. \qquad (7)$$

Hence, the Marangoni number takes the role of a Peclet number for species transport. The above equation is supplemented by the no-flux condition of the solute at the substrate and the condition that the polymer does not evaporate at through the free interface, which is written as

$$\frac{1}{M}\nabla\omega.\boldsymbol{n} = E\omega. \qquad (8)$$

3.2. Numerical approach

3.2.1. Galerkin finite-element formulation

The direct numerical solution of the coupled set of the full equations was based on the Galerkin finite element method. Since the flow domain is changing in time and needs to be found as part of the solution, the ALE (Arbitrary Lagrangian–Eulerian) [39] formulation was adopted. Only a few basic features of the formulation and implementation are presented here for reasons of completeness. Periodic conditions in the direction parallel to the substrate were employed. The laterally periodic domains bounded by the substrate and the moving interface were tessellated into elements of quadrilateral shape. Within each element, the velocities and solute concentration were represented by biquadratic shape functions, whereas the pressure was represented by bilinear functions (Taylor–Hood elements, [40]). The interface was discretized by a set of points equi-spaced in the direction parallel to the substrate, thus representing the local film thickness. In the ALE formulation a grid velocity conforming to the boundary velocity needs to be found. This velocity was taken to have only a vertical component (in the direction towards the substrate) and a magnitude proportional to the vertical velocity of the interface and the vertical position of the grid point. Symbolically, if y is the coordinate of a grid point, h the local thickness and h_t its rate of change, then the grid velocity is

$$\boldsymbol{v}_G = h_t \frac{y}{h}\boldsymbol{e}_y \qquad (9)$$

If φ is a test function from the solute concentration function space, the weak form of the solute transport equation in the ALE formulation may be written:

$$\int_\Omega \frac{\partial \omega}{\partial t}\varphi dV + \int_\Omega [(\boldsymbol{u} - \boldsymbol{v_G}).\nabla\omega]\varphi dV = -\frac{1}{M}\int_\Omega \nabla\omega.\nabla\varphi dV + E\oint_S \phi\omega dS. \qquad (10)$$

To obtain the above form the diffusive terms have been integrated according to Green's theorem and the interfacial flux condition is employed to introduce the last term in the right-hand-side in place of the interfacial diffusive flux.

Similarly, if $\boldsymbol{v}$ is a test function from the velocity space, the weak form of the momentum equations reads

$$0 = \int_\Omega p\nabla.\boldsymbol{v}dV - 2\int_\Omega \mu \boldsymbol{Du} : \boldsymbol{Dv}dV + \oint_S \{[(\frac{1}{Ca} + \omega)\nabla.\boldsymbol{n}]\boldsymbol{n} + \nabla_s\omega\}.\boldsymbol{v}dS, \qquad (11)$$

where, again, the interfacial stress condition has been employed to introduce the last term in place of the components of the stress tensor. Here, $\boldsymbol{Du} = 1/2(\boldsymbol{\nabla u} + \boldsymbol{\nabla u}^T)$ is the rate of deformation tensor.

3.2.2. A second-order-accurate time integration scheme

A procedure to integrate the above equations together with the kinematic condition with 2nd-order accuracy in time is now briefly outlined. This is largely based on the discussion presented by Lucca and Formaggia [41], where more information may be found. After discretizing Eq. (10) in space according to the approach mentioned above, namely with the Taylor–Hood elements, but retaining the differential form in time one obtains the abstract form:

$$\boldsymbol{M}(t)\frac{d\boldsymbol{\omega}}{dt} + \boldsymbol{C}(\boldsymbol{u}, \boldsymbol{v_G}, t).\boldsymbol{\omega} = -\frac{1}{M}\boldsymbol{L}(t)\boldsymbol{\omega} + E\boldsymbol{S_1}(t)\boldsymbol{\omega}. \qquad (12)$$

Here ω is the vector of discrete unknown concentrations, $\boldsymbol{M}$, $\boldsymbol{C}$, $\boldsymbol{L}$ are the so-called mass, convection, Laplace matrices, and $\boldsymbol{S_1}$ is a matrix containing the interfacial contributions. Since the domain is deforming, these matrices are functions of time. Similarly, the momentum equation may be written

$$\boldsymbol{L}_2(\mu, t)\boldsymbol{u} = \boldsymbol{G}(t)p + \boldsymbol{S}_2(\omega, t)\boldsymbol{u}, \qquad (13)$$

where $\boldsymbol{u}$ is the vector of unknown velocities, $\boldsymbol{L_2}$ is a matrix analogous to the Laplacian accounting for the viscous terms with variable viscosity, and $\boldsymbol{G}$, $\boldsymbol{S_2}$ are the pressure gradient and the interfacial stress matrices, respectively.

Suppose now that we have calculated the film thickness, the concentration and the velocity field at an instance in time, say t_n. The time advancement scheme starts with finding the new interface position at $t_{n+1} = t_n + dt$. This is done by integrating the kinematic conditions with a 2nd-order in time explicit scheme. For this purpose, the spatial derivatives of the film thickness are expressed by finite-differences and 3rd-order upwinding is applied.

The next step is to advance the concentration field. Integrating equation (12) over the time interval (t_n, t_{n+1}) and evaluating the mass and diffusive terms implicitly and the rest of the terms explicitly, one may write with 2nd-order accuracy in time:

$$\boldsymbol{M}(t_{n+1/2})\frac{\boldsymbol{\omega}_{n+1} - \boldsymbol{\omega}_n}{dt} + \frac{1}{M}\boldsymbol{L}(t_{n+1/2})\frac{1}{2}(\boldsymbol{\omega}_{n+1} + \boldsymbol{\omega}_n) = \frac{3}{2}[\boldsymbol{C}(\boldsymbol{u}, \boldsymbol{v_G}, t_n) + E\boldsymbol{S}_1(t_n)]\boldsymbol{\omega}_n - \frac{1}{2}[\boldsymbol{C}(\boldsymbol{u}, \boldsymbol{v_G}, t_{n-1}) + E\boldsymbol{S}_1(t_{n-1})]\boldsymbol{\omega}_{n-1} \qquad (14)$$

Thus, the mass and Laplace matrices need to be evaluated at an intermediate level within the time step by interpolating between the domains at t_n and t_{n+1}.

The time advancement scheme is completed by solving Eq. (13) together with the continuity equation for the velocity $\boldsymbol{u}_{n+1}$ and the pressure. Since no time derivatives are involved here and the concentration and the domain have already been advanced, all the terms refer to the time level t_{n+1} and there is no truncation error

in time. The solution is obtained by a coupled Uzawa algorithm where the conjugate gradient method is employed to find the velocity corrections during the iterations. The curvature and normal vector to the interface that are needed in this substep are obtained by employing cubic splines.

4. Results and discussion

In the numerical simulations the functional relationship of viscosity vs. concentration was taken to be the same as obtained from the experimental measurements (cf. Fig.1) and the initial polymer volume fraction was 0.05. The parameter range covered was M = 3000–40000, Ca = 0.05–0.5, while E was kept fixed at a value of 5×10^{-4}. The duration of most simulations was up to 1000 dimensionless time units, which corresponds to the reduction of the film thickness to half of its original height and doubling of the average polymer concentration in the film. It was found that by that time, the velocities developed had slowed down significantly and the patterning of the solute had reached a quasi-steady distribution.

The above conditions were manageable in terms of computational resources and time, but significantly milder than the experimental ones, which range as $M \sim 10^5 - 2 \times 10^6$, $E \sim 10^{-5}$–10^{-4}, and $Ca \sim 0.01$–0.02. However, under these conditions the high Marangoni numbers demand exceedingly fine spatial resolution, the small capillary numbers demand very small time steps because the interfacial deformation problem is numerically stiff, and, finally, the small evaporation numbers require simulations over extended time spans to cover the evolution of the evaporation process. It is therefore suggested that the numerical results may serve to obtain a qualitative understanding of the main processes and mechanisms rather that to reproduce quantitatively the actual experiments. In this respect, it should be kept in mind that the simulations are 2-dimensional in space. For instance, in the experimental configuration corresponding to Fig. 2, wrinkling can be observed at about 25,000 dimensionless time units.

4.1. Free surface deformation

4.1.1. Effect of capillary and Marangoni numbers

In Fig. 5 a measure of surface deformation is presented as a function of time for three capillary numbers and various Marangoni numbers. The first and most important observation to be made is that deformation reaches an overall magnitude that is proportional to the capillary number. This parameter has therefore a dominant effect. At the lowest capillary number, the deformation does not exceed a few percent through the course of the simulation. The numerical results therefore are in accord with the intuitive expectation that strong capillary forces prevent interfacial deformation. Hence, the results suggest that film deformation cannot be the dominant reason of patterning and wrinkling.

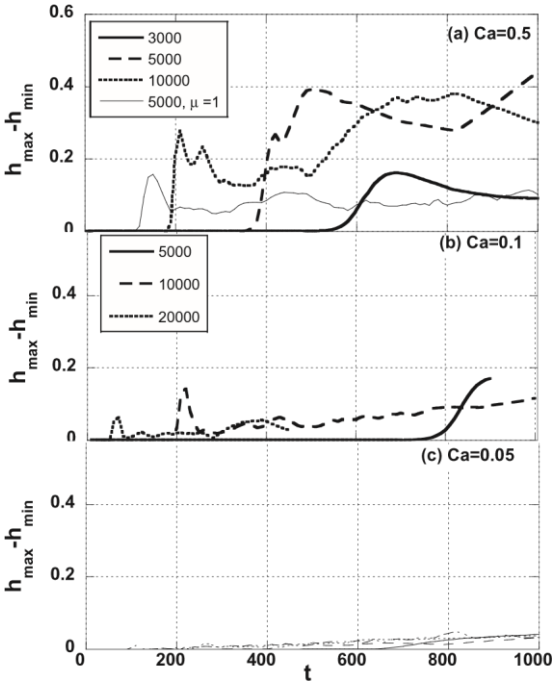

Fig. 5. Effect of the capillary number on interfacial deformation as of function of time for Ca = 0.5 (a), Ca = 0.1 (b) and Ca = 0.05 (c) and various Marangoni numbers.

To illustrate the effects of capillary and Marangoni numbers, Fig. 6 shows the evolution of concentration contours through the course of drying for M = 10,000, Ca = 0.5 and 0.1 on the one hand, Ca = 0.1, M = 10,000 and M = 20,000 on the other hand. The immediate effect of evaporation is that vertical concentration gradients develop. This is simply the result of the selective evaporation that is promoting solvent depletion in the liquid near the interface and is initially counteracted only by bulk diffusion. At high Ca number, the small resistance of the interface to deformation promotes a rapid collection of the concentrated top layer and a significant deformation of the interface is observed with the formation of two lenses at t = 200, which are still visible at t = 1000. We also observe the appearance of secondary structures that are consumed continually by the larger and more permanent ones. This is a feature of Marangoni instability observed in several thermocapillary or solutocapillary systems [1,43].

Decreasing Ca inhibits the interface deformation. The formation of plumes, as for example in the contours for M = 10,000 and t = 300, 400, entrain the concentrated solute from the interface back to the bulk. In this way mixing of the solute takes place, which, in a sense, reduces the driving force and counteracts the deformation process.

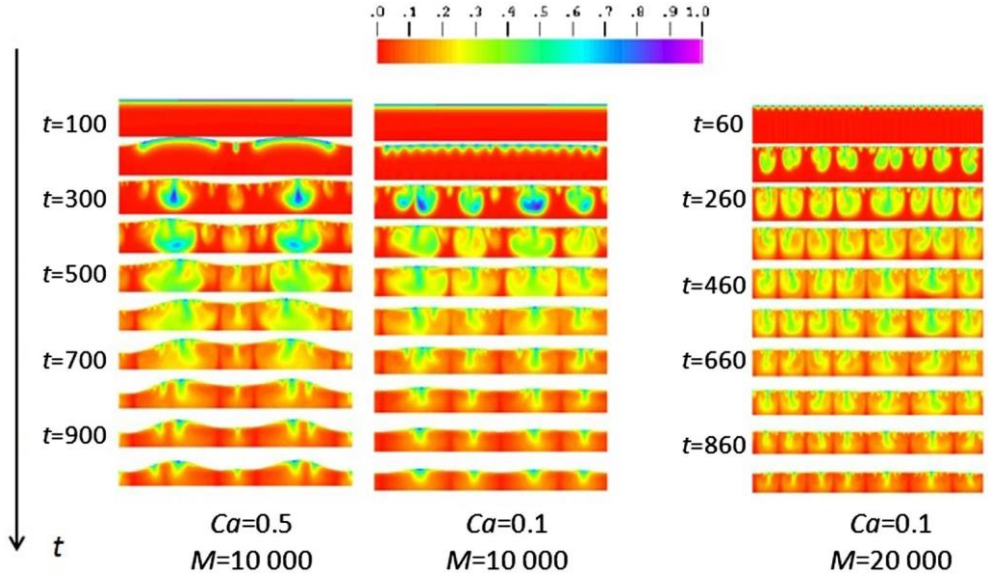

Fig. 6. Successive snapshots of solute concentration contours. The lateral periodic domain size is 4π. In the arbitrary chromatic scale shown on top, 1 corresponds to the instantaneous maximum concentration and 0 to the minimum.

A more detailed sequence of concentration contours for M = 10,000 in Fig. 7 shows this behavior more clearly. In the interval t = 180–210 the sudden growth in deformation observed in Fig. 5b is related to the nonlinear growth of the instability. Right after t = 220 the sudden drop clearly coincides with the initiation of plume formation. A similar effect is observed for M = 20,000 at an even earlier time (cf. Fig. 5b).

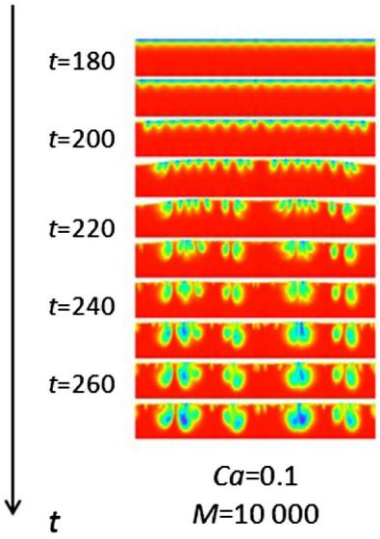

Fig. 7. Solute concentration contours for M = 10,000 and Ca = 0.1, showing initiation of plumes. Successive snapshots at time instants 180, 190, ... ,270. The lateral periodic domain size is 4π.

A second effect is also evident by examining the sequence of concentration contours for two different Marangoni numbers, M = 10,000 and M = 20,000 in Fig. 6. At M = 20,000 finer cells appear at an earlier time, which again tend to cluster and then form plumes plunging back into the bulk. Now the motion is strong enough so that more plumes per unit length are able to survive the coarsening process. Therefore, the distance between the final cells is smaller and capillary forces may be more effective in resisting the deformation of the film. Compatible with the above picture is the result for the deformation in a simulation with constant viscosity, as shown in Fig. 5a. The fluid motion is not inhibited since the viscosity does not increase with solute concentration and hence the tendency of plume formation and the resistance to clustering are increased. Both these effects counteract film deformation.

4.1.2. Comparison with order of magnitude analysis

The order of magnitude analysis is based on previous results detailed in [26,27]. It corresponds to steady regime and constant viscosity assumptions. The additional assumptions and scaling derivation are detailed in Appendix A. The amplitude δh of free surface deformation reads

$$\delta h \sim Ca\, M^{1/3}\, E^{2/3} \qquad (15)$$

The results of the simulations clearly support the conclusion that deformation decreases as the capillary number gets smaller, in agreement with the scaling law (Eq. (15)). Regarding the overall effect of the Marangoni number, a clear conclusion cannot be drawn because this would require more simulations as the exponent in the power law is only 1/3. However, it may be suggested that film deformation due to its overall small magnitude cannot be the dominant reason of patterning and wrinkling, especially as the capillary number in the experiments is less than 0.02.

4.2. Solute Distribution along the film

4.2.1. Effect of Marangoni number

We now turn to the distribution of the solute along the film and examine whether non-uniformities could account for film patterning. For this purpose, the simulations at the lower capillary number of 0.05 where film deformation is small are examined in more detail. The main features obtained from these simulations with increasing Marangoni number are highlighted in Fig. 8, where solute concentration contours are shown again at various instances during film drying. Note that due to increased numerical resolution demands and computational cost limitations, in these simulations the lateral periodic domain size was selected to be 2π. To facilitate comparison with similar plots (Figs. 6,7 and 9) two adjacent periodic cells are drawn for each case.

As may be seen, at the relatively low Marangoni number of 3000 the instability is barely able to develop and induce shearing and deformation of the thickening layer of concentrated solute near the interface. In this way this layer collects into lenses, thus making possible the non-uniformity in the solute distribution. As the Marangoni number is increased, finer cellular structures appear at an ever earlier stage and coalesce into big structures. Beyond that phase, within the large established structures smaller secondary ones continue to appear at large M almost throughout the entire simulation. These secondary structures become constantly consumed by the already established large permanent formations. The process is similar to what is seen in 3D simulations [42–43]. Up to M = 20,000 the number of the final cells remains the same, whereas at M = 40,000 their number increases. From all the above results it may be suggested that the increase in the strength of the Marangoni forces promotes the instability, the clustering of cells and the non-uniformity of solute distribution. However, again and in direct analogy with the discussion on film deformation there appear to be subtle effects for the same reasons. Stronger plumes result in enhanced mixing of the solute and finer structures are able to survive the process of coalescence.

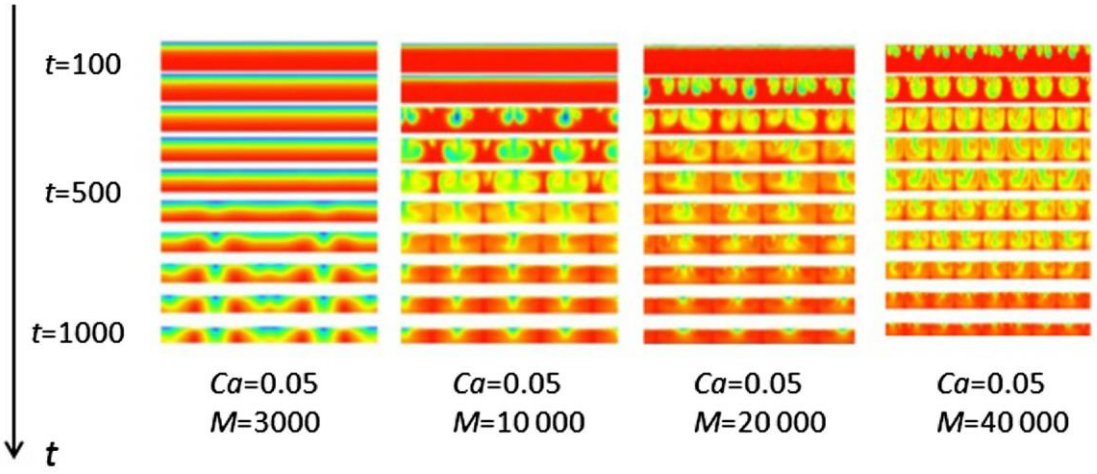

Fig. 8. Successive snapshots of solute concentration contours at time instants 100, 200, ... ,1000. The lateral domain size shown is 4π.

It may be argued here that since the structures finally remaining after cessation of coalescence are more than one in the periodic domains there is no artifact of the size of the lateral domain where periodic conditions are imposed. However, to further test such effects one simulation was repeated with the lateral domain size doubled and it was shown that the dynamics and number of final structures per unit lateral length are not affected.

4.2.2. Effects of the varying viscosity

To examine the effect of the varying viscosity on the distribution of solute along the film, similar simulations were performed where the viscosity was kept constant, independent of solute concentration. The capillary number and the evaporation number in these simulations were the same and the Marangoni number ranged between 5000 and 20,000. The development of the instability may be observed through the evolution of concentration contours during drying, as is shown in Fig. 9.

The main events are similar. A notable difference by comparing Figs. 8 and 9 is that the instability appears at an even earlier stage and the number of final structures is higher after the process of cell coalescence and coarsening. The differences with the variable viscosity simulations are more pronounced at relatively lower Marangoni numbers.

Not unexpectedly, when the viscosity is constant the overall magnitude of the velocities is larger and it is sustained for a longer period during drying, as may be seen by comparing the data in Fig. 10. When the viscosity is varying the velocities are smaller, here by a factor in the range 2–5, which depends on the Marangoni number.

A related important difference is in the characteristics of the velocity field, a sample of which is shown in Fig. 11. The large arrows in this figure indicate interfacial points of maximum solute concentration. When the viscosity is constant, the downward motion is strong at the points corresponding to high concentrated regions, thus promoting mixing. The opposite happens when the viscosity increases with concentration. The downward motion almost vanishes at the points of maximum concentration.

The same kind of behavior was observed experimentally by Bassou and Rharbi during drying of PS/toluene solutions. Indeed, using trajectory of probe particles to visualize the flow, they obtained quasi immobile zones between the convective cells.

All the above features suggest that the effect of viscosity is significant in promoting the non-uniformity of the solute distribution along the film. In contrast to the constant viscosity case, where the higher velocities at the points corresponding to maximum concentration promote sustained mixing, the increasing viscosity inhibits convection and mixing of the solute back to the bulk. Indeed, this may also be observed from the solute concentration probability density distributions, shown in Fig. 12, all corresponding to dimensionless time, t = 1000, when roughly half of the solvent has been removed. For constant viscosity these distributions are symmetric around the mean value of 2 (relative to the initial concentration), they are relatively narrow and not significantly affected by the Marangoni number. In contrast, the distributions for the variable viscosity case are skewed and have extended tails towards values larger than the average. This is the result of asymmetry between upward and downward motion promoted by the increasing viscosity.

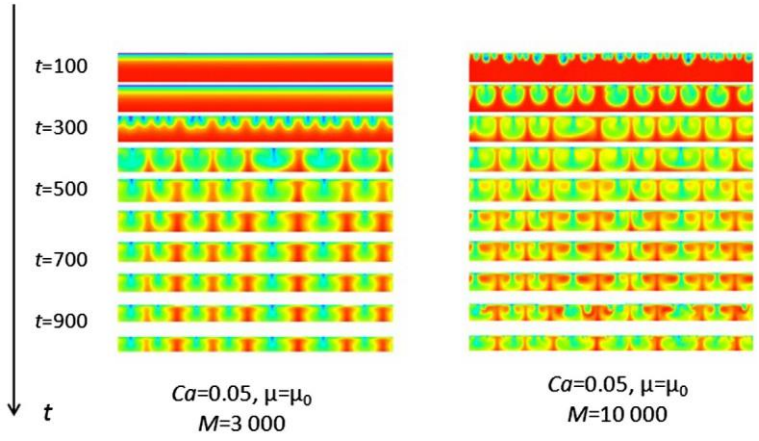

Fig. 9. Solute concentration contours for constant viscosity and M = 3000 (left), M = 10,000 (right). Successive snapshots at time instants 100, 200, ... ,1000. The lateral periodic domain size is 4π.

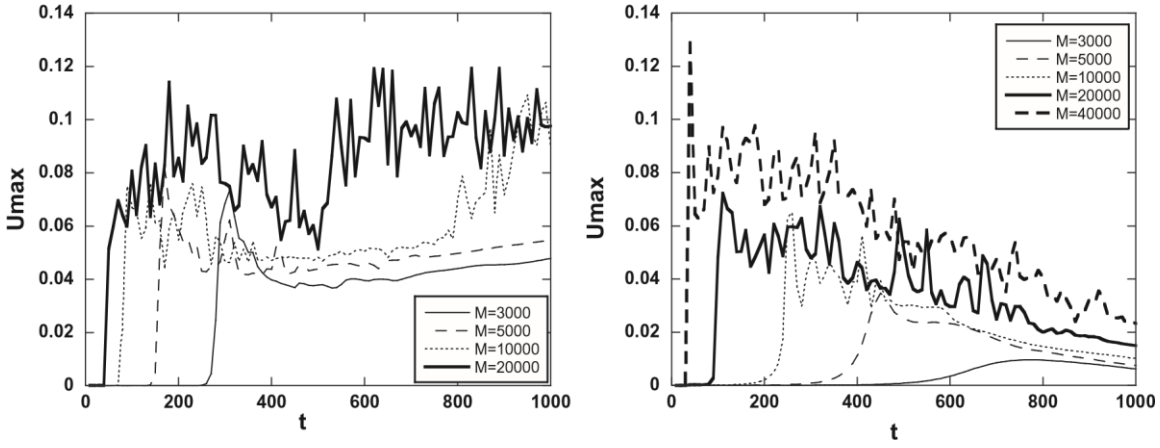

Fig. 10. Maximum velocity for constant (left) and varying viscosity (right) as a function of time for various Marangoni numbers.

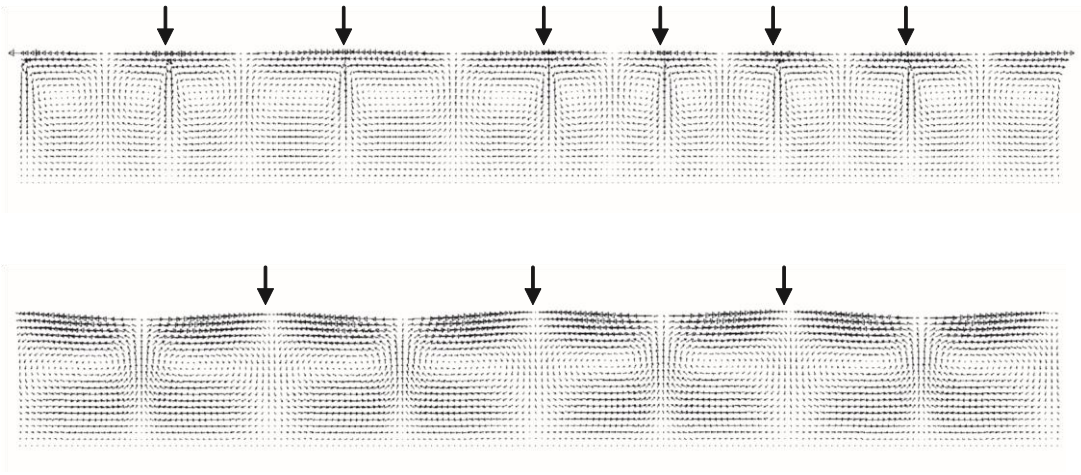

Fig. 11. Map of instantaneous velocity vectors for Ca = 0.05, M = 5000 at t = 1000, for constant (top) and varying viscosity (bottom). The lateral periodic domain size is 4π.

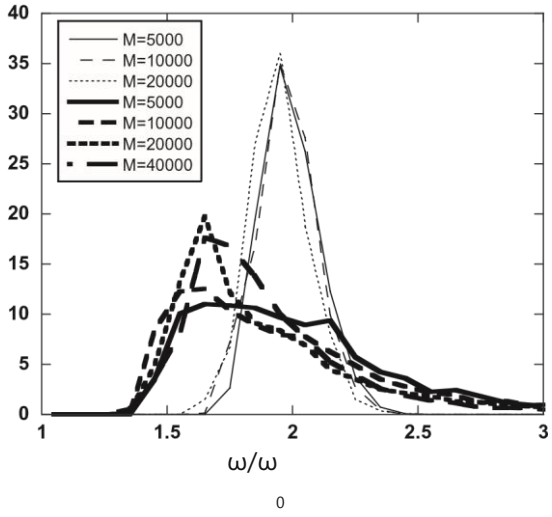

Fig. 12. Probability density distribution of solute concentration in the film at time t = 1000 for various Marangoni numbers, Ca = 0.05. Thicker lines are for varying viscosity and thinner for constant viscosity.

4.2.3. Patterning of the dried film due to solute lateral non-uniformity

Given all the previous observations, it appears plausible to suggest that the non-uniformity in the solute distribution is a significant effect and could be responsible for the final patterning of the dried films. During the late stages of drying evaporation would certainly become affected by concentration and mainly come from the more dilute parts of the interface. Motion would also be significantly slowed down and the diffusivity of the solvent would decrease dramatically. Whereas these effects may not be easily simulated, it may be argued that diffusion would not be able to restore the concentration uniformity in the remaining film because it would require a relative time scale much larger than O(M).

As a measure of solute lateral non-uniformity, the vertically averaged solute content was calculated as a function of position along the substrate and of time. This vertically averaged polymer content, which is scaled with the initial mean concentration, also represents a measure of the remaining dry film thickness if the solvent were instantaneously removed. The evolution of the standard deviation of this measure of dry thickness with time is shown in Fig. 13. It is clear from this figure that the distribution has reached a steady regime for t > 200 for the cases of constant viscosity. A very different behavior is observed for the cases of variable viscosity, where some regions become more concentrated while others stay diluted (the evaporation rate being constant in the simulations, the mean solute concentration is the same for variable or constant viscosity). No steady regime is observed for variable viscosity all along the drying, which results in an accumulation phenomenon inducing spatial variation of polymer concentration much larger than in the constant viscosity case.

If it is assumed, therefore, that the simulations capture, at least qualitatively, the final solute distribution, then an estimate of the final film thickness non-uniformity may be obtained by the distribution of the vertically averaged solute content at the end of the simulations. The relevant probability density distributions at t = 1000 along the film are shown in Fig. 14. Compared to the constant viscosity case these distributions are wider and skewed towards values smaller than the average.

The trends are also evident by examination of some statistical parameters for various Marangoni numbers, as shown in Table 1. Notably, excursions above the mean are more pronounced and the effect of the varying viscosity is clear.

If we therefore plot the projected final film thickness along the interface we obtain the results shown in Fig. 15. Significant variations appear in the final thickness, of the order of the mean value, and this occurs only when the viscosity is taken to vary with the solute concentration. This is in agreement with orders of magnitude

obtained in experiments. Indeed, for PS/toluene solutions, Bassou and Rharbi obtain about 0.25 for the ratio of the average corrugation amplitude to the average dry film thickness. For the PIB/toluene experiments described in Section 2, standard deviation is about 0.28.

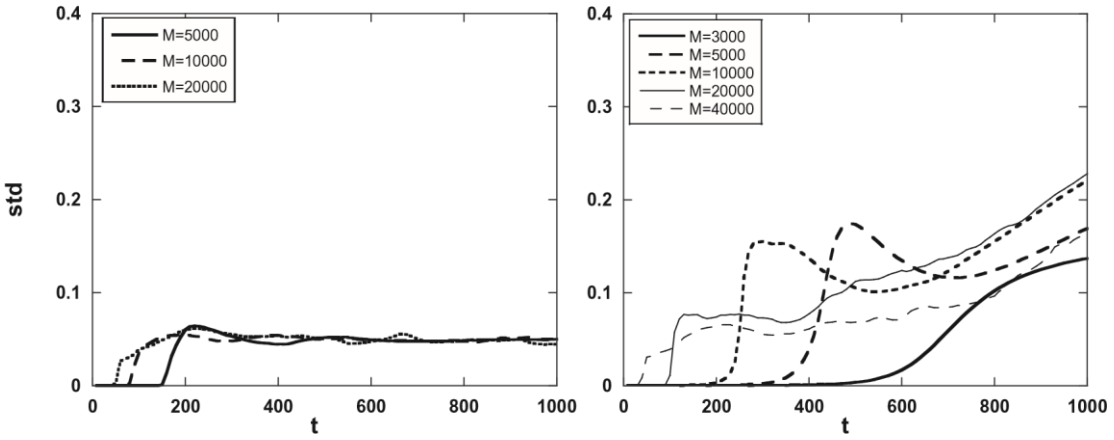

Fig. 13. Standard deviation of the vertically averaged solute content as a function of time for constant (left) and variable viscosity (right), for various Marangoni numbers, Ca = 0.05.

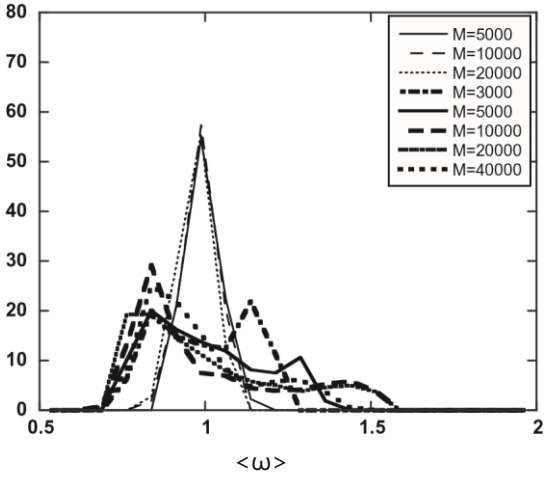

Fig. 14. Probability density distribution of vertically averaged solute content or dry film thickness, at time t = 1000 for various Marangoni numbers, Ca = 0.05. Thicker lines are for varying viscosity and thinner for constant viscosity. The data are normalized to have a mean value of unity.

Table 1. Statistical parameters of the dried film on the basis of the solute lateral distribution. The data are normalized to have a mean value of unity for the dry film thickness h_{dry}.

M	Dry film thickness for variable viscosity			Dry film thickness for constant viscosity		
	$h_{dry\text{-}min}$	$h_{dry\text{-}max}$	Standard deviation	$h_{dry\text{-}min}$	$h_{dry\text{-}max}$	Standard deviation
3000	0.79	1.19	0.14	0.90	1.11	0.050
5000	0.75	1.33	0.17	0.89	1.14	0.050
10,000	0.73	1.53	0.22	0.86	1.09	0.049
20,000	0.72	1.54	0.23	0.85	1.06	0.045
40,000	0.73	1.40	0.16			

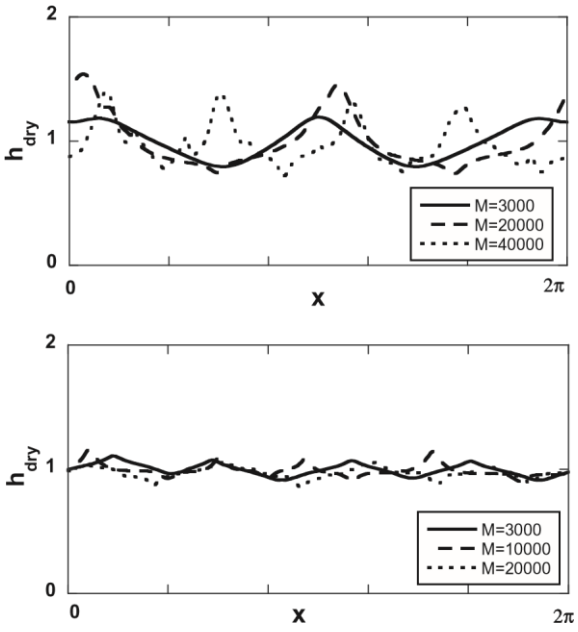

Fig. 15. Thickness of the dried film on the basis of the solute lateral distribution for varying (top) and constant viscosity (bottom) and various Marangoni numbers, at time t = 1000 and Ca = 0.05.

5. Concluding remarks

The purpose of the present paper is to shed light through numerical simulations on the potential mechanisms that cause permanent wrinkling of dried polymer films. Solutal Marangoni phenomena are considered. First, simulations show that free surface deformation induced by capillary pressure reaches an overall magnitude that is proportional to the capillary number, in agreement with scaling analysis. Decreasing *Ca* inhibits the interface deformation through the formation of plumes that helps mixing of the solute. For the value of capillary number corresponding to experiments, free surface deformation is not significant. The other mechanism investigated is the non-uniformity of solute concentration induced by Bénard–Marangoni convection. Comparisons of simulations with constant and varying viscosity suggest that the effect of viscosity is significant in promoting the non-uniformity of the solute distribution along the film and leads to accumulation of solute that is observed up to the end of the simulation. When the solute concentration is high enough, velocity decreases due to high viscosity and the system is frozen. Resulting corrugation amplitudes are in agreement with experiments. Therefore, though simulations have been performed with dimensionless numbers significantly milder than the experimental ones, they confirm the mechanism proposed by Bassou and Rharbi [5], i.e. wrinkles may be viewed as the signature of Bénard–Marangoni convection.

Conflict of interest

None declared.

Acknowledgements

F.D. and B.G. thank ANR EVAPEC 13-BS09-0010-01 for funding. S.G.Y. thanks the University Paris-Sud for funding as a visiting professor.

Appendix A.

Based on simplifying assumptions, scaling laws have been obtained by ‘‘solving’’ equations of solutal model in terms of order of magnitude. All the equations below must be hence understood as orders of magnitude only since these scalings do not give prefactors. We use results previously obtained in [26,27], where scaling analysis on the solutal problem led to a partition in five domains of the different configurations, characterized by the values of the non-dimensional parameters. For each domain, the thicknesses of hydrodynamic boundary layer and solutal boundary layer, the velocity and concentration variation have been derived from scaling analysis and expressed as a function of Marangoni and Evaporation numbers. Based on these results, we analyze here the relative importance of inertia and viscous term, and derive the scaling law for free surface deformation. The following assumptions are used:

H1. Below the free surface, we assume the existence of a hydrodynamic and a solutal boundary layer.
H2. Time derivative terms are neglected (quasi-steady regime).
H3. Solvent concentration variations across a convective cell in the vertical and horizontal directions are of the same order of magnitude.
H4. The wavelength of convective structures scales with the layer thickness. Hence the order of magnitude of the dimensionless characteristic length in the horizontal direction is one.
H5. The analysis is restricted to fluids characterized by a Schmidt number greater than one.
H6. Viscosity and layer thickness are assumed constant and equal to their initial values.

It can be shown that the configurations used in the numerical simulations performed in this paper belong to the domain called ‘‘B’’ in the scaling analysis performed in [27] (cf. Table 3 and Fig. 11 in this reference). Indeed, with the definition of Marangoni and evaporation numbers used in this paper, this region is limited by the following boundaries:

$1 << M^2 E << Sc^{3/2}$ and $M E^2 << 1$. It is easy to check that the values used in the simulations (M = 3000–40,000, $E = 5\times10^{-4}$, $Sc = 2\times10^5$) obey to these three criteria. In this domain, the hydrodynamic layer is of the order of one and the velocity scales as $M^{1/3} E^{2/3}$ [27].

A.1. Inertia versus viscous terms

Using the above results, it is possible to compare the inertia and viscous terms in the Navier-Stokes equation (1) governing the fluid motion.

u and v being the velocity components in the horizontal and vertical directions, mass conservation with the above velocity scaling reads

$$u \sim v \sim M^{1/3}\, E^{2/3} \qquad \text{(A-1)}$$

In the steady regime and assuming constant viscosity, the ratio between inertia terms (lhs of Eq. (1)) and viscous terms (rhs of Eq.(1)) is therefore of the order of $M^{4/3} E^{2/3} Sc^{-1}$.

According to Fig. 11 and Table 4 of [27], with the definition of Marangoni number used here, ‘‘B’’ region verifies $M^2 E << \mathrm{Sc}^{3/2}$. Thus, the ratio between inertia terms and viscous terms is much less than one, which means that viscous terms are dominant for the configurations studied.

A.2. Scaling analysis for free surface deformation

Free surface deformation is assumed small and small slope approximation is used in the following. No distinction is made between the vertical direction and the normal to the free surface. The curvature is taken as the second derivative of the thickness and is of the order of $\delta h / \lambda^2$, where δh and λ are the amplitude and wavelength of deformation, respectively. Thus, normal stress balance at the interface reads in dimensionless form

$$\Gamma_{nn} \sim (Ca^{-1} + \omega)\, \frac{\delta h}{\lambda^2} \qquad \text{(A-3)}$$

with Γ_{nn} the normal stress at the interface. Using $\Gamma_{nn} \sim \Gamma_{yy}$, with assumption H4 ($\lambda \sim 1$) and in the range of capillary numbers used in the simulations, Eq. (A-3) reads

$$\Gamma_{yy} \sim Ca^{-1}\, \delta h \qquad \text{(A-4)}$$

Disregarding inertia terms in Navier-Stokes equation, Eq. (1) in the vertical direction reads

$$\frac{\partial \Gamma_{yy}}{\partial y} = -\frac{\partial \Gamma_{yx}}{\partial x} = -\frac{\partial}{\partial x}\left(\frac{\partial v}{\partial x} + \frac{\partial u}{\partial y}\right).$$

The hydrodynamic layer being of the order of one in the ‘‘B’’ domain, and using Eq. (A.1) and assumption H.4, the order of magnitude for the normal stress reduces to

$$\Gamma_{yy} \sim u \sim M^{1/3}\, E^{2/3}. \qquad \text{(A-5)}$$

From (A-4) and (A-5) it follows:

$$\delta h \sim Ca\, M^{1/3}\, E^{2/3}.$$

References

[1] M.F. Schatz, G.P. Neitzel, Experiments on thermocapillary instabilities, Ann. Rev. Fluid Mech. 33 (2001) 93.
[2] L.E. Scriven, C.V. Sternling, The Marangoni effects, Nature 186 (1960) 187.
[3] O.E. Jensen, J.B. Grotberg, The spreading of heat or soluble surfactant along a thin liquid film, Phys. Fluids A 5 (1) (1993) 58.
[4] A. Abbasian, S.R. Ghaffarian, N. Mohammadi, M.R. Khosroshahi, M. Fathollahi, Study of different planforms of paint’s solvents and the effect of surfactants (on them), Prog. Org. Coatings 49 (2004) 229.
[5] N. Bassou, Y. Rharbi, Role of Bénard–Marangoni Instabilities during Solvent Evaporation in Polymer Surface Corrugations, Langmuir 25 (2009) 624.
[6] S.G. Yiantsios, B.G. Higgins, Marangoni flows during drying of colloidal films, Phys. Fluids 18 (2006) 082103.
[7] S.G. Yiantsios, B.G. Higgins, A mechanism of Marangoni instability in evaporating thin films due to soluble surfactant, Phys. Fluids 22 (2010) 022102.
[8] S.K. Serpetsi, S.G. Yiantsios, Stability characteristics of solutocapillary Marangoni motion in evaporating thin films, Phys. Fluids 24 (2012) 122104.
[9] S.Y. Heriot, R.A.L. Jones, An interfacial instability in a transient wetting layer leads to lateral phase separation in thin spin-cast polymer-blend films, Nature Mater. 4 (2005) 782.
[10] P. Colinet, J.C. Legros, M.G. Velarde, Nonlinear Dynamics of Surface-TensionDriven Instabilities, Wiley-VCH, 2001.
[11] J.R.A. Pearson, On convection cells induced by surface tension, J. Fluid Mech. 4 (1958) 489–500.
[12] L.E. Scriven, C.V. Sternling, On cellular convection driven by surface-tension gradients: effect of mean surface tension and surface viscosity, J. Fluid Mech. 19 (1964) 321–340.
[13] J. Reichenbach, H. Linde, Linear perturbation analysis of surface tension driven convection at a plane interface, J. Colloid Interface Sci. (1981).
[14] D.A. Goussis, R.E. Kelly, On the thermocapillary instabilities in a liquid layer heated from below, Int. J. Heat Mass Transfer 33 (1990) 2237–2245.
[15] S.H. Davis, Thermocapillary instabilities, Ann. Rev. Fluid Mech. 19 (1987) 403. [16] A. Oron, S.H. Davis, S.G. Bankoff, Long-scale evolution of thin films, Rev. Mod. Phys. 69 (1997) 931.
[17] R.V. Craster, O.K. Matar, Dynamics and stability of thin liquid films, Rev. Mod. Phys. 81 (2009) 1131.
[18] H. Mancini, D. Maza, Pattern formation without heating in an evaporative convection experiment, Europhys. Let. 66 (2004) 812.
[19] C. Moussy, G. Lebon, J. Margerit, Influence of evaporation on Bénard– Marangoni instability in a liquid-gas bilayer with a deformable interface, Eur. Phys. J. B 40 (2004) 327–335.
[20] D.P. Birnie, D.M. Kaz, D.J. Taylor, Surface tension evolution during early stages of drying of sol–gel coatings, J. Sol–Gel Sci. Technol. 49 (2009) 233.
[21] E. Bormashenko, S. Balter, R. Pogreb, Y. Bormashenko, O. Gendelman, D. Aurbach, On the mechanism of patterning in rapidly evaporated polymer solutions: Is temperature-gradient-driven Marangoni instability responsible for the large-scale patterning?, J Colloid Interface Sci. 343 (2010) 602.
[22] K.E. Strawhecker, S.K. Kumar, J.F. Douglas, A. Karim, The critical role of solvent evaporation on the roughness of spin-cast polymer films, Macromolecules 34 (2001) 4669.
[23] P.G. de Gennes, Instabilities during the evaporation of a film: Non-glassy polymer + volatile solvent, Eur. Phys. J. E 6 (2001) 421.
[24] V.M. Ha, C.L. Lai, Onset of Marangoni instability of a two-component evaporating droplet, Int. J. Heat Mass Transfer 45 (2002) 5143–5158.
[25] H. Machrafi, A. Rednikov, P. Colinet, P.C. Dauby, Time-dependent Marangoni– Bénard instability of an evaporating binary-liquid layer including gas transients, Phys. Fluids 25 (2013) 084106.

[26] B. Trouette, E. Chenier, F. Doumenc, C. Delcarte, B. Guerrier, Transient Rayleigh–Bénard–Marangoni solutal convection, Phys. Fluids 24 (2012) 074108.
[27] F. Doumenc, E. Chénier, B. Trouette, T. Boeck, C. Delcarte, B. Guerrier, M. Rossi, Free convection in drying binary mixtures: solutal versus thermal instabilities, Int. J. Heat Mass Transfer 63 (2013) 336.
[28] W.S. Overdiep, The leveling of paints, Prog. Org. Coatings 14 (1986) 159.
[29] S.D. Howison, J.A. Moriarty, J.R. Ockendon, E.L. Terrill, S.K. Wilson, A mathematical model for drying paint layers, J. Eng. Math. 32 (377) (1997).
[30] M.H. Eres, D.E. Weidner, L.W. Schwartz, Three-dimensional direct numerical simulation of surface-tension-gradient effects on the leveling of an evaporating multicomponent fluid, Langmuir 15 (1999) 1859.
[31] Cerda, L. Mahadevan, Geometry and physics of wrinkling, Phys. Rev. Let. 90 (074302) (2003).
[32] Soumendra K. Basu, L.E. Scriven, L.F. Francis, A.V. McCormick, Mechanism of wrinkle formation in curing coatings, Prog. Org. Coatings 53 (1) (2005).
[33] C.-M. Chen, S. Yang, Wrinkling instabilities in polymer films and their applications, Polym. Int. 61 (2012) 1041.
[34] L. Xue, J. Zhang, Y. Han, Phase separation induced ordered patterns in thin polymer blend films, Prog. Polym. Sci. 37 (2012) 564.
[35] S. Xu,M.Li, Z.Mitov,E.Kumacheva, Surface textures induced by convection in thin films of polymeric and polymerizable fluids, Prog. Org. Coatings 48 (2003) 227.
[36] J. Jaczewska, A. Budkowski, A. Bernasik, E. Moons, J. Rysz, Polymer vs solvent diagram of film structures formed in spin-cast Poly(3-alkylthiophene) blends, Macromolecules 41 (2008) 4802.
[37] S. Sakurai, K. Tanaka, S. Nomura, Highly organized macroscopic pattern observed on the free surface of a polymer film cast from a solution, Macromolecules 25 (1992) 7066.
[38] F. Doumenc, B. Guerrier, C. Allain, Mutual diffusion coefficient and vapor liquid equilibrium data for the system PIB/Toluene, J. Chem. Eng. Data 50 (2005) 3.
[39] L.-W. Ho, A.T. Patera, A Legendre spectral element method for simulation of unsteady incompressible viscous free-surface flows, Comput. Methods Appl. Mech. Eng. 80 (1990) 355.
[40] H. Elman, D. Silvester, A. Wathen, Finite Elements and Fast Iterative Solvers, Oxford University Press, New York, 2006.
[41] Formaggia, F. Nobile, Stability analysis of second-order time accurate schemes for ALE–FEM, Comput. Methods Appl. Mech. Eng. 193 (2004) 4097.
[42] T. Kollner, K. Schwarzenberger, K. Eckert, T. Boeck, Multiscale structures in solutal Marangoni convection: Three-dimensional simulations and supporting experiments, Phys. Fluids 25 (2013) 092109.
[43] K. Schwarzenberger, T. Köllner, H. Linde, T. Boeckb, S. Odenbach, K. Eckert, Pattern formation and mass transfer under stationary solutal Marangoni instability, Adv. Colloid Interface Sci. 206 (2014) 344.